Tribology International 188 (2023) 108866

Contents lists available at ScienceDirect

Tribology International

journal homepage: www.elsevier.com/locate/triboint

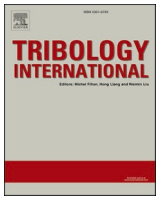

2D Spring-block model to study the transition from static to kinetic friction of complex-micro-textured contact surfaces

S.K. Jalali [a], N.M. Pugno [a,b,*]

[a] Laboratory for Bio-Inspired, Bionic, Nano, Meta Materials & Mechanics, Department of Civil, Environmental and Mechanical Engineering, Università di Trento, via Mesiano, 77, I-38123 Trento, Italy
[b] School of Engineering and Materials Science, Queen Mary University of London, Mile End Road, London E1 4NS, UK

ARTICLE INFO

Keywords:
Stick-slip
Micro-/nano-scale Friction
Texture
Microslip

ABSTRACT

The capability of complex micro-texturing technique for tuning the transition from static to kinetic friction is investigated based on a two-dimensional (2D) lattice spring block model. Results reveal that implementation of micro-texturing remarkably decreases the static friction coefficient even for a small amount of covering percentage, however this effect gets slight after covering percentage of about 10%. It is observed that elongation of micro-texturing cavities perpendicular to the sliding direction can improve its reducing effect on static friction coefficient. Furthermore, as simulations prove, using complex shapes of micro-texturing cavities with sharp vertexes slightly modifies the frictional response.

1. Introduction

Friction is the resistance to motion experienced when one body is moving over another. As a subdomain of tribology, it is known as one of the oldest practical topics in science and technology due to its central importance in determining the efficiency and functionality of many manmade devices for everyday life applications dealing with surface contacts. Despite intensive studies since ancient times by outstanding scientists, e.g., Leonardo da Vinci, Amontons and Coulomb (AC), summarized as "Amontons-Coulomb constitutive laws of friction" [1–3], various aspects are still open as a result of multiscale complex nature of interface between bodies in relative motion. In spite of the simplicity of classical AC laws of friction, they can predict the transition from stick to slip in a sharp sense, stating that no sliding occurs as long as the ratio of the shear force to the normal load remains below a threshold known as the static friction coefficient. This assumption divides the sliding friction timeline into two regimes, i.e., the static (pre-sliding) friction and the kinetic (dynamic) friction regime. Transferring from the former to the latter demands for formation and propagation of micro-sliding at the interface which precedes the macro-sliding of the bodies in contact. The classic AC friction formulation has the limitation of constants friction coefficients, although has been proved to be valid under certain conditions for many couples of materials in contact, however, the modified formulations like rate-and-state friction law [4,5] are suggested to consider the dependency of friction coefficients to sliding velocity and sliding duration.

In many realistic contacting surfaces, in addition to the micro-scaled surface roughness, presence of intrinsic or artificial meso- and/or macro-scaled patterning significantly affects the characteristics of the contact offering an extra degree of freedom for tunability. This phenomenon has been widely observed in biological contacting systems commonly in the form of hierarchical patterning, e.g., gecko paw [6,7], insect legs [8], and human skin [9]. This supports the idea of bioinspired surface patterning for optimal designs considering the fact that both maximizing and minimizing the friction coefficients are demanded, as the friction is not always a nuisance like tires and brakes of cars. Experimental investigations [10–12] and numerical simulations at molecular levels [13] have confirmed the successful manipulation of friction by the implementation of different geometries of artificial surface patternings in both dry and wet slidings. On the other hand, recent developments in modern chemical [14] and physical [15] techniques for pattern implementation, from nano to macro scales in combination with multi-material 3D printing facilities [16,17], have provided a unique platform for realization of these optimal designs.

Among different choices for simulating the phenomenon of transition from static to kinetic friction regimes and predicting the effect of surface patterning on the frictional response in both local and global

* Corresponding author at: Laboratory for Bio-Inspired, Bionic, Nano, Meta Materials & Mechanics, Department of Civil, Environmental and Mechanical Engineering, Università di Trento, via Mesiano, 77, I-38123 Trento, Italy.
E-mail address: nicola.pugno@unitn.it (N.M. Pugno).

https://doi.org/10.1016/j.triboint.2023.108866
Received 30 June 2023; Received in revised form 23 July 2023; Accepted 9 August 2023
Available online 10 August 2023

Nomenclature

l	Dimension of discretizing block
A_{tot}	Total sliding area
A_{tex}	Micro-textured area
Γ	Micro-textured zone
(x,y)	Coordinate of sliding plan
(x_0,y_o)	Origin of micro-textured zone
(x_Γ,y_Γ)	Boundary of micro-textured zone
λ	Size parameter of micro-textured zone
φ	Angle parameter of micro-textured zone
s	Edge parameter of micro-textured zone
w	Sharpness parameter of micro-textured zone
N_x	Number of discretizing blocks along x
N_y	Number of discretizing blocks along y
N	Total number of discretizing blocks
E	Young's modulus of the slider
ρ	Density of the slider
ν	Poisson's ratio of the slider
$\boldsymbol{V}$	Sliding velocity vector
V_x	Velocity component along x
V_y	Velocity component along y
P	Total pressure on the slider
Ω	Damping parameter
Ω_c	Critical damping parameter
k_1	Spring constant of straight neighbors
k_2	Spring constant of diagonal neighbors
k_s	Spring constant of applying velocity
F_{ni}	Normal force on block i
m_i	Mass of block i
N_s	Number of sliding blocks
d_{ij}	Initial distance between blocks i and j
$\boldsymbol{u_0}$	Initial location of blocks
$\boldsymbol{u}$	Location of blocks
$\dot{\boldsymbol{u}}$	Velocity of blocks
$\boldsymbol{F_{si}}$	Sliding force on block i
$\boldsymbol{F_{fi}}$	Friction force on block i
$\boldsymbol{F_{ci}}$	Internal force on block i
$\boldsymbol{F_{di}}$	Damping force on block i
$\boldsymbol{a}$	Acceleration of blocks
τ_c	Contacting stress
$\tau_c^{\max}$	Maximum contacting stress
t	Time
Δt	Time step
t_T	Total sliding time
t_s	Transition time
μ	Friction coefficient
μ_s	Static friction coefficient (c.)
μ_k	Kinetic friction c.
$\overline{\mu}_s$	Local static friction c. (mean)
$\overline{\mu}_k$	Local kinetic friction c. (mean)
$\overline{\sigma}_s$	Local static friction c. (standard deviation)
$\overline{\sigma}_k$	Local kinetic friction c. (standard deviation)
μ_{si}	Local static friction c. of block i
μ_{ki}	Local kinetic friction c. of block i
t^*	Dimensionless time
Δt^*	Dimensionless time step
t_T^*	Dimensionless total sliding time
t_s^*	Dimensionless transition time
V^*	Dimensionless velocity
R^*	Dimensionless kinetic to static friction ratio
Ω^*	Dimensionless damping
τ_c^*	Dimensionless contacting stress
μ^*	Dimensionless friction coefficient
μ_s^*	Dimensionless static friction coefficient
μ_k^*	Dimensionless kinetic friction coefficient
σ_s^*	Dimensionless static deviation
σ_k^*	Dimensionless kinetic deviation
N^*	Percentage of sliding blocks
A^*	Percentage of micro-texturing area

points of views, the lattice spring-block model has been cited as an efficient approach thanks to its simplicity and flexibility for overcoming the inherent complexities of simulating rough patterned surfaces as well as considering dependencies of the applied sliding velocity and normal pressure. Capozza and Urbakh [18] established a 1D spring-block model for understanding how and why the values of static friction coefficient can vary within wide limits and proposed a relationship between measured values of static friction and pre-slip stress profiles at the frictional interface and predict how the range of variation of the static friction depends on material properties and on the size of the slider. Amundsen et al. [19] suggested a 1D spring-block model to develop an analytical prediction for the length of precursors as a function of the applied tangential load and correlated the microscopic and macroscopic friction coefficients in the model. It allowed for robust comparison with experimental observation of stick-slip motion. An elastic 2D spring-block vertical model, where the bottom layer of blocks is in frictional interaction with the substrate, was proposed in [20] and a mechanism for slow slip was revisited and it was demonstrated that fast slip and fast fronts have a different inertial origin; it was also revealed how both the local shear to normal stress ratio and the local stiffness are involved in the selection of front type and front speed. Costagliola et al. [21] proposed a 2D lattice spring-block model to evaluate the effect of surface patterning in form of arrays of cavities and pillars on the frictional properties of elastic sliding surfaces and it was shown how friction can be effectively tuned by appropriate design of such surface features. In addition, using the same model they investigated the correlation between slip precursors and topological length scales at the onset of frictional sliding in [22] and it was found that different types of detachment sequences are triggered by specific surface structures, depending on their scales and relation to sliding direction, leading to a macroscopically smooth transition to sliding in the case of hierarchical and/or anisotropic features. Berardo et al. [23] experimentally and numerically investigated the effect of surface patterning on the adhesive friction properties of polymer surfaces. They introduced a modified 2D spring-block which considers the local adhesion, and the effect of sliding velocity is implemented and a good agreement between the experiment and the numerical simulation was observed. The numerical prediction of frictional coefficients of composite hierarchical surfaces was carried out in [24] applying a 1D spring-block model with a heterogenous network of springs and it was shown that a remarkable reduction of static friction can be achieved by introducing hierarchical arrangements of varying local roughness values, or by introducing controlled material stiffness variations. Using numerical simulations based on a graded version of 2D spring-block model, Guarino et al. [25] investigated how graded material properties affect the macroscopic frictional behavior, in particular, static friction values and the transition from static to dynamic friction, and the results suggested that the graded material properties can reduce static friction, opening possibilities for the design of bioinspired surfaces with tailor-made tribological properties. Implementing the 1D spring-block model presented in [26] for surfaces with grooves, Costagliola et al. [27] studied the effect of hierarchical surface patterning on the static and dynamic friction coefficients of an elastic material and

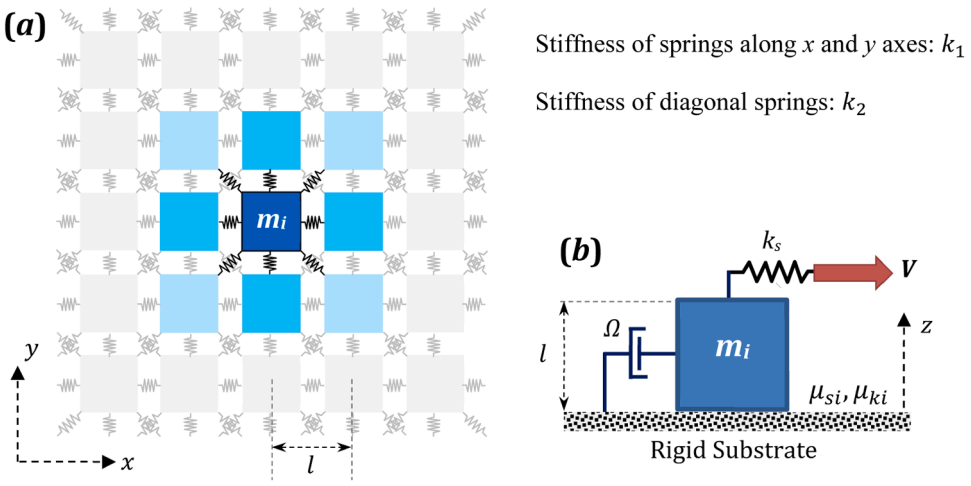

Fig. 1. : The Schematic of the lattice spring-block model of the discretized contacting surface.

some possible mechanisms that explain how hierarchical structures can significantly modify the friction coefficients of materials were highlighted, providing a means to achieve tunability. Since the contact of two surfaces in relative rotating motion occurs in many practical applications, from mechanical devices to human joints, recently, a rotating version of 2D spring-block model was extended to study friction between surfaces in torsional contact in [28] and it was investigated how the model describes the behavior of an elastic surface slowly rotating over a rigid substrate, comparing results with an analytical calculation based on energy balance.

The present work first presents a comprehensive parametric study on the 2D spring-block model developed for simulation of transition from static to kinetic friction in [21] to explain the effect of both internal parameters including the properties of mass-damper-spring network and the statistical parameters of local friction coefficients and external parameters, i.e., sliding velocity, normal pressure, and the correlation between them through a dimensionless form. Then, the capability of complex-micro-texturing for tuning the transition behavior from static to kinetic friction is discussed in detail considering the effect of size, orientation, and shape of micro cavity patterns. The finding of this study along with recent developments in the technologies of micro-texturing, such as engraving by Femto-lasers, offers a guidance for designing and optimizing real-world applications from macro-scale mechanical components to MEMS devices. It can lead to tuning friction coefficient and improving overall performance of the parts on the contact.

2. Problem definition

2.1. Lattice spring-block model

Emerging from conventional computational approaches, including frame network methods, molecular dynamics, and discrete element methods, the lattice-spring model stands as one of the pioneering simulation techniques successfully employed in solid mechanics. Due to its distinct physical representation, it has found widespread application across diverse domains, however, for specific fields, the model is tailored through necessary adjustments. The version of lattice-spring model employed in the study of friction is more known as block-spring model. The dynamic nature of sliding necessitates the inclusion of lumped masses which are represented as sliding blocks in the model. It enables the transmission of contact-induced loads through localized frictional interactions of the blocks.

In present work, the two-dimensional (2D) lattice spring-block model [21,29] is used to investigate the effect of micro-texturing on the dry frictional behavior of elastic sliders based on the classical AC friction force assumptions [30] applying on discretized local contacting subareas. One can find a detail description of the model in [21]. Consider an elastic slider of Young's modulus E and density ρ in contact to a rigid substrate under uniform total pressure P distributed on the total sliding area A_{tot} and driven by a constant velocity V parallel to the contacting surface. The plane x-y is laid on the contacting surface while the z axis is perpendicular to the sliding plane. Being a multiscale fractal phenomenon, the asperity size of contacting surfaces can be considered from nano- to meso-scale [31,32] aligning with the scale we have investigated. Regarding the size of asperities of a mesoscale contacting area is in the order of microns [33] and keeping in mind that the applied textures for tuning the tribological properties of surfaces using current techniques like femto-lasers are in the range of microns, the contact surface is uniformly meshed by a square element of size l equals to 1 μm to guaranty the suitable mesh resolution. In fact, the continuous contacting surface is replaced by a finite number of contact points. Here, the number of contacting points in both in-plane direction i.e., N_x, and N_y are chosen identical and hence their total number in the mesh, N, is $N_x^2 = N_y^2$. Since the problem is modeled in two dimensions, the thickness of the slider is an arbitrary parameter setting equals to l i.e., 1 μm to form a mesh of cubes for discretizing the whole slider.

In the lattice spring model, the total mass of slider is distributed on the lumped masses, m_i, located at the center of subareas. A network of linear springs, consisting of two kinds of linear springs k_1 (aligned with the x and y axes), and k_2 (diagonal), connects every block to its eight adjacent blocks. It is noted that, limiting the connections to the adjacent blocks, the long-range interactions that may arise from wave propagation are neglected; however, many researchers have reported the effective implementation of such lattice spring-block model for studying the transition from static to kinetic friction at least for low sliding velocities [34–36]. Besides, diagonal springs are adopted in the model for bringing the Poisson's effect in the simulation. It is shown that by setting the spring constants $k_1 = 0.75El$, and $k_2 = 0.375El = 0.5k_1$, this spring network can mimic accurately the Young's modulus of the slider but accepting the limitation of a non-adjustable Poisson's ratio of $\nu = 1/3$ [37]. To consider the shear rigidity of the slider, the sliding velocity is applied to blocks through an elastic connection of stiffness $k_s = k_2$ [21]. Furthermore, to control the artificial oscillations of the mass-spring network, a damper is also inserted [26]. The schematic of lattice spring model is depicted in Fig. 1.

The final step to establish the model is to define the contacting interaction between the slider and the rigid substrate. Every block has a local contact point and behaves individually based on classical AC force. It means block i needs a local static, μ_{si}, and a local kinetic, μ_{ki}, friction coefficients. These friction coefficients are chosen statistically using a

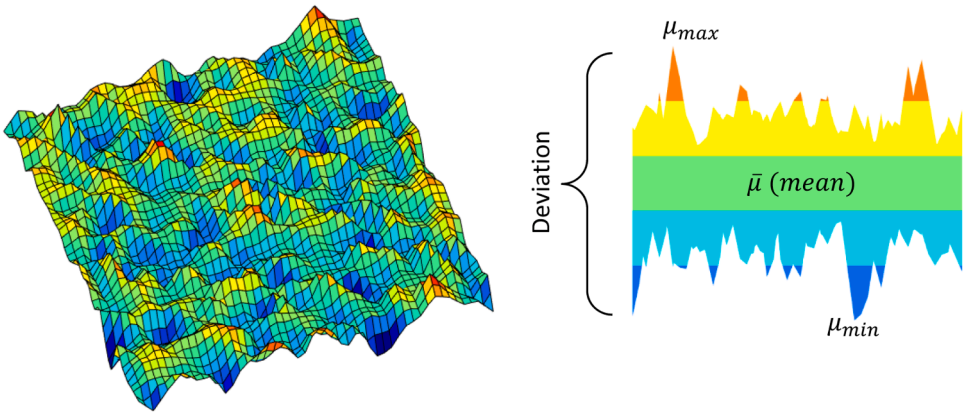

Fig. 2. : A schematic of the variation of local friction coefficients distributed on the contact surface based on a random Gaussian function.

random Gaussian distribution as follows:

$$g(\mu_{si}) = \frac{\exp(-(\mu_{si} - \bar{\mu}_s)^2/2\bar{\sigma}_s^2)}{\sqrt{2\pi}\bar{\sigma}_s} \tag{1a}$$

$$g(\mu_{ki}) = \frac{\exp(-(\mu_{ki} - \bar{\mu}_k)^2/2\bar{\sigma}_k^2)}{\sqrt{2\pi}\bar{\sigma}_k} \tag{1b}$$

where $\bar{\mu}_s$, $\bar{\mu}_k$, $\bar{\sigma}_s$ and $\bar{\sigma}_k$ are the mean values and standard deviations, respectively. Fig. 2 represents an example of random distribution of local static and kinetic friction coefficients. It is supposed that the zone exposed to micro-texturing are not in contact with the substrate. Hence, this surface modification is considered in the simulation by setting to zero the local friction coefficients of the blocks located on the zones removed by micro-texturing.

2.2. Resultant forces

During the simulation, the block i, with initial rest position $\boldsymbol{u_0}$ and the current position $\boldsymbol{u}(t)$, experiences different forces in the plane of sliding i.e., x-y plane. First, the sliding force, $\boldsymbol{F_{si}}(t)$, from the shearing spring is:

$$\boldsymbol{F_{si}}(t) = k_s(\boldsymbol{u_0} + \boldsymbol{V}t - \boldsymbol{u}(t)) \tag{2}$$

Second, the resultant of internal forces, $\boldsymbol{F_{ci}}(t)$, from the springs connected to the adjacent blocks is:

$$\boldsymbol{F_{ci}}(t) = \sum_{j=1}^{n_a} k_c(u_{ij} - d_{ij})\boldsymbol{e_{ij}}(t), \; c \quad = 1 \; or \; 2 \tag{3}$$

where n_a is the number of adjacent blocks, k_c is the stiffness of connecting spring between blocks i and j (k_1 or k_2), u_{ij} is the current distance of blocks i and j, d_{ij} is the rest distance of blocks i and j (l or $\sqrt{2}l$), and $\boldsymbol{e_{ij}}(t) = (\boldsymbol{u_j}(t) - \boldsymbol{u_i}(t))/u_{ij}$ is the unit vector oriented from block i to block j.

Third, the friction force, $\boldsymbol{F_{fi}}(t)$, from the contact point of the substrate obeys the classical AC friction force. The total normal force acting on the slider, F_n, is given by multiplying the applied normal pressure, P, by the apparent total area, A_{tot}. Then, the normal force acting on the block i, F_{ni}, is obtained by uniform distribution of F_n on the blocks which are in contact to the substrate. Note that the blocks located within the surface textured zone are not in contact with the substrate and therefore do not carry the normal load. The normal force on the blocks, F_{ni}, is assumed to be constant during the simulation. As long as the block i is at rest, i.e., static friction phase, the friction force balances the total applied load up to the threshold value defined by multiplying the normal force acting on the block, F_{ni}, by the local static friction coefficient, μ_{si}. After exceeding the threshold, a constant kinetic friction force in the opposite direction of movement of block i is applied, whose magnitude is obtained by multiplying F_{ni} by μ_{di}:

$$\boldsymbol{F_{fi}}(t) = -(\boldsymbol{F_{si}}(t) + \boldsymbol{F_{ci}}(t)) \text{ if } |\boldsymbol{F_{si}} + \boldsymbol{F_{ci}}| \leq \mu_{si}F_{ni} \tag{4a}$$

$$\boldsymbol{F_{fi}}(t) = \mu_{ki}F_{ni}\dot{\boldsymbol{e}}_i(t) \quad \text{if} \quad |\boldsymbol{F_{si}} + \boldsymbol{F_{ci}}| \rangle \mu_{si}F_{ni} \tag{4b}$$

where $\dot{\boldsymbol{e}}_i(t) = \dot{\boldsymbol{u}}_i(t)/|\dot{\boldsymbol{u}}_i(t)|$ is the unit vector of the velocity of block i. The fourth one is the damping force, $\boldsymbol{F_{di}}(t)$, from the damper of damping parameter Ω.

$$\boldsymbol{F_{di}}(t) = -\Omega m_i \dot{\boldsymbol{u}}_i(t) \tag{5}$$

The resultant force acting on block i can be calculated as:

$$\Sigma\boldsymbol{F}_i(t) = \boldsymbol{F_{si}}(t) + \boldsymbol{F_{ci}}(t) + \boldsymbol{F_{fi}}(t) + \boldsymbol{F_{di}}(t) \tag{6}$$

2.3. Solution procedure

From the numerical solution point of view, the present study is classified as a discontinues simulation, a sub-discipline of Computational Mechanics. For performing such a simulation, there is a variety of approaches like discrete element methods [38], molecular dynamics methods [39], etc., however, the main idea is time discretization of the governing equations of the system followed by explicit time integration schemes. These methods discretize the system to a network of interacting lumped masses and implement the Newton's law of motion to obtain the velocity and displacement of the ith particle from the unbalanced forces applied to it. In Sections 2.1 and 2.2, discretization procedure and definition of interacting forces for the present study of elastic slider is explained in detail. The main goal of simulation is to solve the governing equation of motion, i.e., Newton's law, for all consisting blocks of the elastic slider on the time period of $t \in [0, t_T]$ divided by the time step Δt. The acceleration of every particle, $\boldsymbol{a}_i(t)$, can simply be calculated by dividing the resultant force in Eq. (6) by the mass of particle:

$$\boldsymbol{a}_i(t) = \Sigma\boldsymbol{F}_i(t)/m_i \tag{7}$$

The time integration is performed based on a finite-difference scheme, called the 'velocity-Verlet' algorithm [39] to update the position, $\boldsymbol{u}_i$, and the velocity, $\dot{\boldsymbol{u}}_i$, of every individual block i as follows:

$$\boldsymbol{u}_i(t + \Delta t) = 2\boldsymbol{u}_i(t) - \boldsymbol{u}_i(t - \Delta t) + \boldsymbol{a}_i(t)(\Delta t)^2 \tag{8a}$$

$$\dot{\boldsymbol{u}}_i(t + \Delta t) = \dot{\boldsymbol{u}}_i(t) + \boldsymbol{a}_i(t)\Delta t \tag{8b}$$

Considering the updated positions and velocities, the components of acting forces on blocks is updated through Eqs. (2–5). Having these, one can investigate the frictional behavior of the contacting surface e.g., for studying the transition from static to kinetic phase.

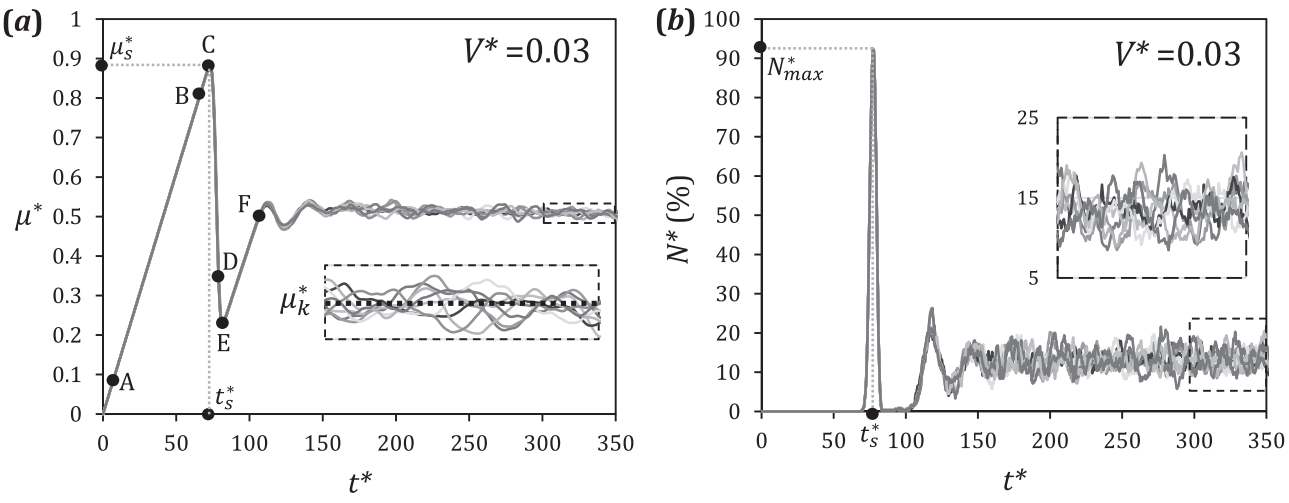

Fig. 3. : Transition from static to kinetic phase with respect to dimensionless time, t^*, for $V^*= 0.03$, $N= 625$, $R^*= 0.5$, $\Omega^*= 0.1$, and $\sigma_s^*=\sigma_k^*= 0.05$. *a*) dimensionless static coefficient, *b*) percentage of sliding blocks.

3. Results and discussion

In this section, a comprehensive parametric study on tribological properties of the elastic slider based on lattice spring model is presented. To demonstrate the results, first some parameters need to be defined as the outputs. The friction coefficient, μ, is a global output that is the ratio of resultant sliding force to the total normal force, P, acting on the slider in every moment of simulation, namely:

$$\mu = \left(\sum_{i=1}^{i=N} \boldsymbol{F}_{si}\right)/(PA_{tot}) \tag{9}$$

The static friction coefficient, μ_s, is the maximum value of μ at the transition time, $t=t_s$. The kinetic friction coefficient, μ_k, is estimated by averaging the friction coefficient μ after fully transition to kinetic phase. The number of sliding blocks, having non-zero velocity, is named N_s. The contact stress, τ_{ci}, is defined as a local output for every individual block to study the propagation of sliding through the contact surface:

$$\tau_{ci} = \left|\boldsymbol{F}_{fi} + \boldsymbol{F}_{ci}\right|/l^2 \tag{10}$$

where || denotes the magnitude of the corresponding vector. Furthermore, some dimensionless parameters are introduced to generalize the results:

$$V^* = \frac{\sqrt{E\rho}}{P\overline{\mu}_s}|\boldsymbol{V}|, \Omega^* = \Omega\sqrt{m_i/k_1}, N^* = 100(N_s/N) \tag{11a}$$

$$\left(t^*, \Delta t^*, t_s^*, t_T^*\right) = \sqrt{E/\rho}(t, \Delta t, t_s, t_T) \tag{11b}$$

$$\begin{aligned} &R^* = \overline{\mu}_k/\overline{\mu}_s, \\ &(\mu^*, \mu_s^*, \mu_k^*, \sigma_s^*) = (\mu, \mu_s, \mu_k, \overline{\sigma}_s)/\overline{\mu}_s, \\ &\sigma_k^* = \overline{\sigma}_k/\overline{\mu}_k, \\ &\tau_c^* = \tau_c/\tau_c^{\max} \end{aligned} \tag{11c}$$

$\tau_c^{\max}$ is the maximum value of contact stress during the simulation, then $0 \le \tau_c^* \le 1$. At the next subsections, the results for non-micro-textured and micro-textured surfaces are discussed in detail.

3.1. Non-micro-textured contact surface

In order to make a basic insight into the influence of effective parameters, the dimensionless friction coefficient, μ^*, versus dimensionless time t^* for $R^*= 0.5$, $N= 625$ (N_x=25), $\Omega^*= 0.1$, and $\sigma_s^*=\sigma_k^*= 0.05$ is depicted in Fig. (3*a*). Eight cases, listed in Table 1, having different values of V, P, E, ρ, and $\overline{\mu}_s$ but all resulting in the same value of dimensionless velocity, $V^*= 0.03$, are plotted. The velocity direction is parallel to the axis x. It is seen that for the same value of V^*, the μ^*-t^* plots are identical in the static and the transition phases. Although the plots in the kinetic phase are not exactly coincident point by point, however, they fluctuate around the almost same average value. In Fig. (3*b*) one can see the same behavior for the percentage of sliding blocks. It is concluded that dimensionless velocity can be considered as an effective generalizing parameter in the forthcoming parametric study. However, it should be noted that in the upcoming presented results the values of P, E, ρ, and $\overline{\mu}_s$ parameters are chosen equal to the case no. 8 in Table 1 and different values of V^* achieved only by changing $|\boldsymbol{V}|$. One should pay attention to μ_k^*, μ_s^*, t_s^*, and $N_{\max}^*$ on the graphs.

Table 1
Parameters of eight samples presented in Fig. 3 resulting in $V^*= 0.03$ (R^*=0.5).

Cases	$\|V\|$ [mm/s]	P [kPa]	E [MPa]	ρ [g/cm^3]	$\overline{\mu}_s$ [-]
1	0.0949	0.1	1	1	1
2	0.9490	1	10	0.1	1
3	1.8980	2	0.1	10	2
4	0.9490	0.1	1	0.01	1
5	4.7450	10^3	10^4	4	1
6	0.1898	2	10^3	0.1	3
7	0.9490	10	10^2	1	2
8	0.0949	10^2	10^5	10	1

In Fig. 4, the dimensionless contact stress, τ_c^*, is visualized for the six instants of simulations highlighted by the points from A to F in Fig. (3*a*). Placing this stress under close scrutiny provides significant information about the reasons for transitional behavior from static to kinetic phase: as soon as the simulation starts, obeying Eq. (2), the sliding force is applied to all the blocks resting at their initial location. The internal and damping forces are zero and the local friction force of every block stands against micro sliding. Therefore, the contact stress of all blocks linearly and equally increases. When micro sliding happens, this contact stress reduces suddenly which makes it an evidence for visualizing the microslip phenomenon. This linear increase continues until point B, where the sliding force exceeds the local friction threshhold for the blocks having the lowest values of local static friction coefficient, μ_{si}, and first micro slidings bring up. The movements of these blocks from their initial rest position apply the internal forces through Eq. (3) to the adjacent blocks near to their threshhold. Consecuently, precursory

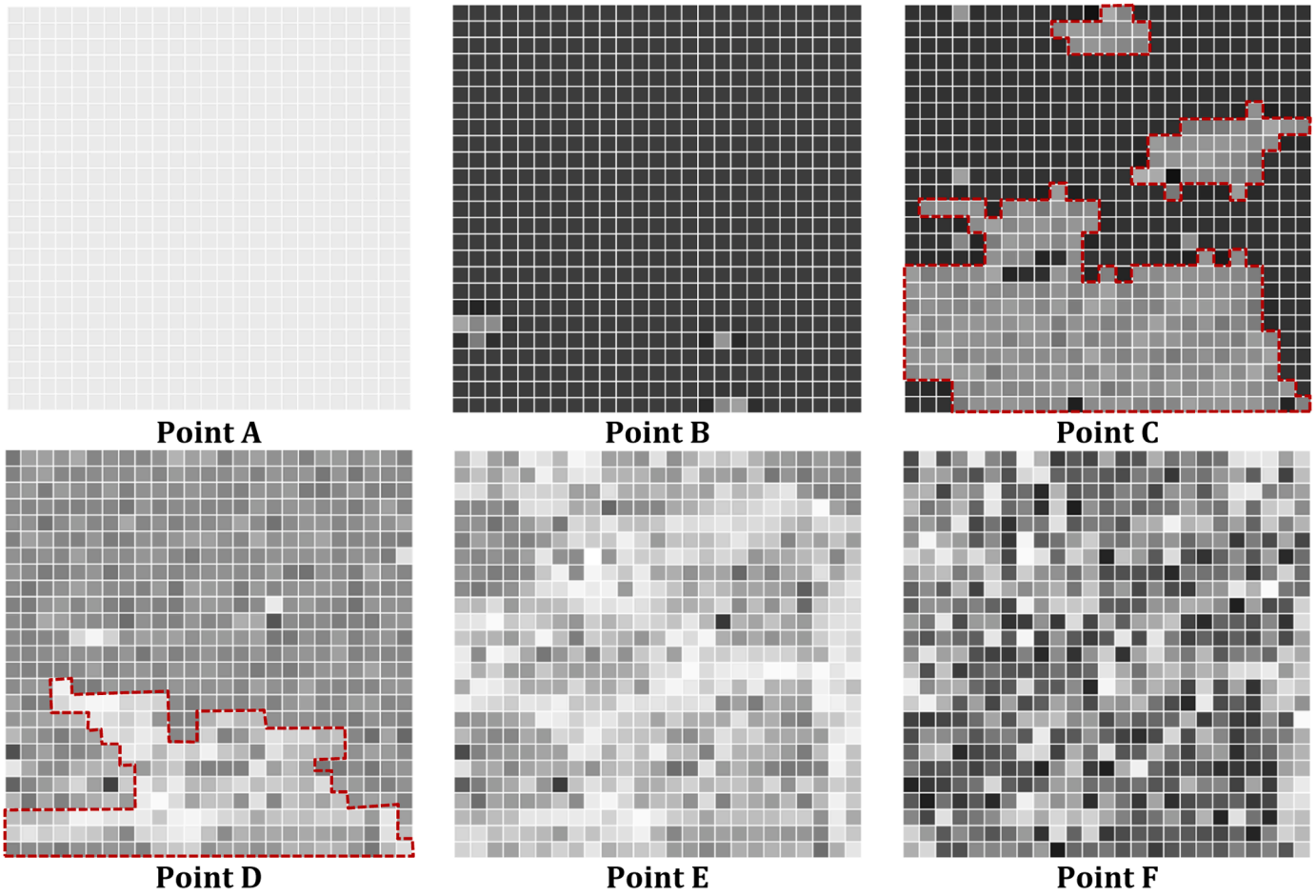

Fig. 4. : Visualization of dimensionless contact stress, τ_c^*, for the six instants of simulations demonstrated by the points from A to F on Fig. (3*a*). Note: □τ_c^*= 0, ■ τ_c^*= 1.

micro slip fronts are formed and start to propagate. It is in agreement with Fig. (3*b*) where the percentage of sliding blocks experiences a sudden increasing peak. It is interesting that at the point C, where the maximum global static friction coefficient is obtained, the micro slip fronts have not covered the whole contact surface yet. Passing point C, the micro slip fronts are fully and quickly propagated on the surface. Regarding point D, a second front of reduction in the contact stress is observed, which is propagated on the whole contact area at point E and corresponds to the lowest value of global friction coefficient. The transition step is followed by the kinetic phase, where the stick-slip phenomenon governs the dynamics of blocks. The contact stresses of blocks at point F is demonstrated as a sample instant of this phase.

Keeping in mind that the size of discretizing blocks are fixed to one micron, a convergence study on the size effect of simulated contacting area is performed to find a proper minimum area (number of blocks) that can realisticly represent a large contacting area. The μ^*-t^* and N^*-t^* plots for three different number of blocks i.e. N= 25, 625, and 5625 corresponding to the total sliding area of A_{tot}= 5 × 5, 25 × 25, and 75 × 75 square microns are depicted in Fig. 5. It is observed that by increasing the contact area, the plots converge rapidly. Although a very small contacting area of 25 square microns seems to show reasonable results, the minimum contacting area of 625 square microns is here considered as a reliable sample to avoid undesired edge effects. Increasing the simulated area directly increases the simulation time, thus the only reason for simulating larger areas is the need of higher resolution for adopting complicated micro-texturing patterns. The distribution of dimensionless contact stress, τ_c^*, is reported in Fig. (5*c*).

Fig. 6 focuses on the effect of dimensionless velocity on the sliding time as well as simulation time. It is observed that the dimensionless sliding time, t_s^*, is inversly proportional to the dimensionless velocity, V^*:

$$t_s^* \cong (5/2)V^{*-1} \tag{12}$$

Regarding definition of V^* in Eq. (11a) it means that for a certain values of Young's modulud E and density ρ, increasing either P or $\overline{\mu}_s$ makes a delay in the sliding time, t_s, while increasing $|V|$ speeds it up. Although increasing the term $\sqrt{E/\rho}$ decreases dimensionless sliding time, t_s^*, from combining Eq. (11a) and Eq. (11b) one can concluded that the Young's modulus does not have any effect on the sliding time, t_s, while increasing density, this increses the inertia of the system and makes a delay in the starting of micro-slidings.

Simulation time is correlated to the time step, Δt. On the other hand, selecting a proper time step supports the stability and convergene of the simulation. From simulations, it is observed that increasing dimensionless velocity, V^*, demands for bigger values of Δt^* to keep the simulation stable. Nevertheless, for high values of V^* it is not possible to find a proper value for Δt^* and the results are fluctuating. Fig. 7 presents the μ^*-t^* and N^*-t^* plots for $V^* = 0.2$ as an example of instability appearance that cannot be fixed by tuning Δt^*. In all upcoming simulations where $0.01 < V^* < 0.2$, the value of Δt^* is set as follow to make a balance between speed and stability of simulation:

$$\Delta t^* = (2/3)V^* \tag{13}$$

One may pay attention that for a slider with a certain number of blocks, the simulation time is explicitly related to the number of time steps needed before the micro-sliding starts, n_s^*, which is obtained by

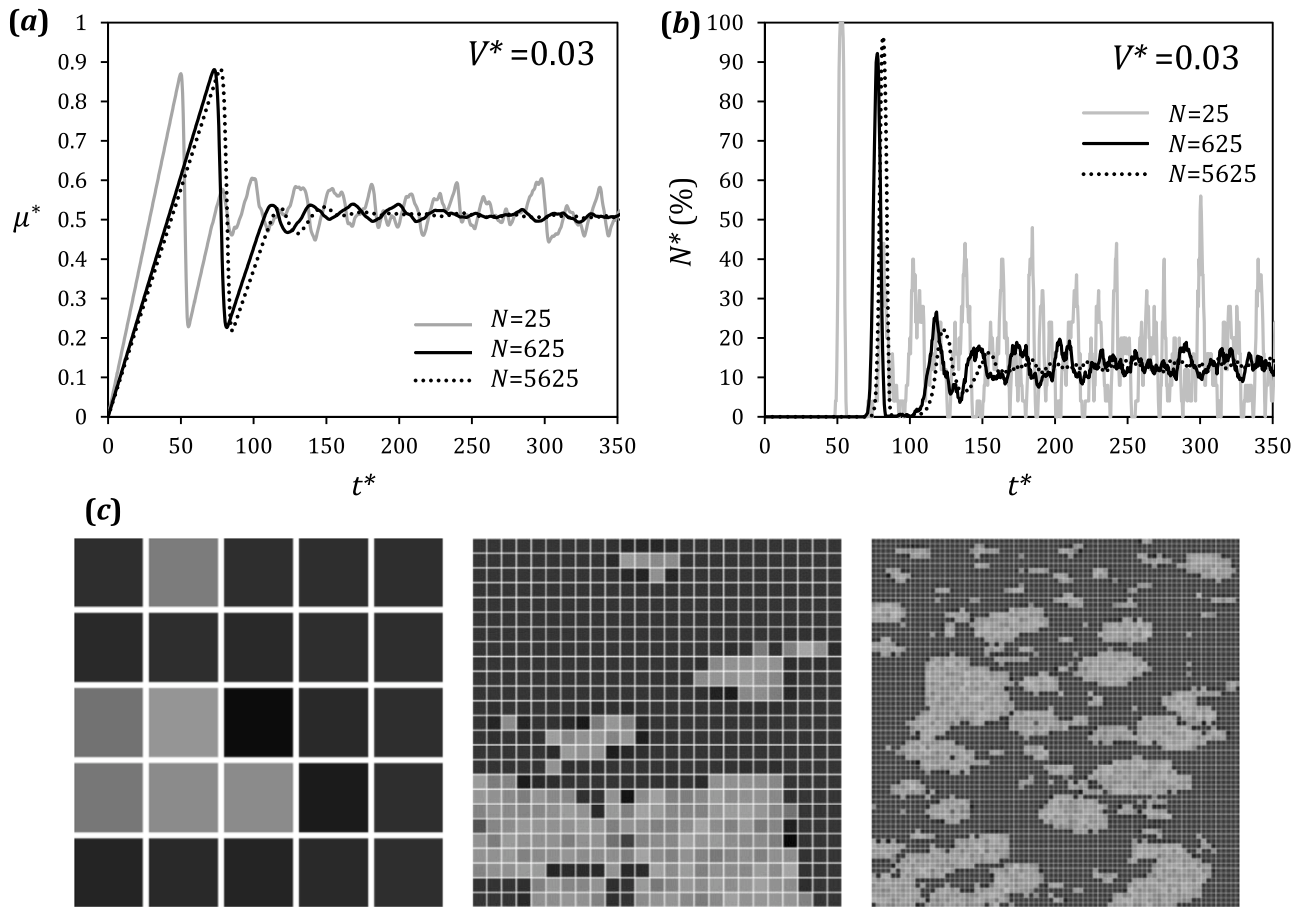

Fig. 5. : Effect of the size of simulated contacting area for $V^*= 0.03$, $R^*= 0.5$, $\Omega^*= 0.1$, and $\sigma_s^*=\sigma_k^*= 0.05$. *a*) dimensionless friction coefficient, *b*) percentage of sliding blocks, *c*) dimensionless contact stress by varying the discretization: □$\tau_c^*= 0$, ■ $\tau_c^*= 1$.

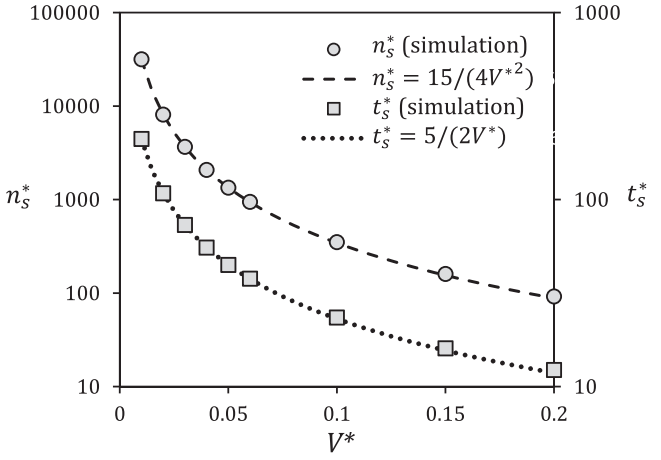

Fig. 6. : The effect of dimensionless velocity on sliding time and simulation time (N=625, R^*=0.5, Ω^*=0.1, and σ_s^*=σ_k^*=0.05).

dividing Eq. (12) by Eq. (13):

$$n_s^* = t_s^*/\Delta t^* = (15/4)V^{*-2} \tag{14}$$

where n_s^* increases dramatically by decreasing the dimensionless velocity, V^*, see Fig. 6 again. For instance, decreseing V^* from 0.05 to 0.01 increases 25 times the simulation duration.

The variation of dimensionless static friction coefficient, μ_s^*, with respect to dimensionless velocity, V^* is denomstrated in Fig. 8. A slight increase is observed tending to $\mu_s^*= 1$. Paying attention to the definition of μ_s^* in Eq. (11c) it means that for high values of V^* the static friction of whole slider is getting closer to the mean value of local static friction of individual blocks, $\overline{\mu}$.

Influence of damping parameter on the transition from static to kinetic phase with respect to dimensionless time, t^*, for $V^*= 0.03$, $N= 625$, $R^*= 0.5$, and $\sigma_s^*=\sigma_k^*= 0.05$ is presented in Fig. 9. It is observed that damping parameter does not affect the static phase unlike the transition and dynamic phases. Increasing damping parameter causes an increase in dynamic friction coefficient, however, for the damping value, Ω, comparable to the frequency of the mass-spring network, $\sqrt{k_1/m_i}$, i.e. Ω^* around 1 and higher, the stick-slip behavior vanishes and all the blocks move toghether, $N^*= 100$. All the upcoming results use $\Omega^*= 0.1$.

In Fig. 10, the μ^*-t^* is depicted for four different values of dimensionless kinetic to static friction coefficient ratio, R^*. It is seen that this ratio dictates how maximum value in static phase and the mean value in the dynamic phase are close; for $R^*= 1$ the transition phase has almost vanished. Besides, for $R^*= 0.5$ and 0.75 the dimensionless kinetic friction coefficient, μ_k^*, is around the mean value of local kinetic coefficient, $\overline{\mu}_k$, while for the low value of $R^*= 0.25$, μ_k^* is lower than $\overline{\mu}_k$.

Fig. 11 compares the distribution of local static friction coefficient, μ_{si}, for starting the propagation of micro-sliding fronts. As it is expected the local minimums of μ_{si}, marked by circles on Fig. (11*a*), are the starting points of micro-sliding. It is concluded that these local minimums lead the transition from static to kinetic phase. Two determinative factors affect the local minimums of μ_{si}: random distribution and dimensionless static standard deviation, σ_s^*, which are related to the topology of real contact surface. The former determines the location of

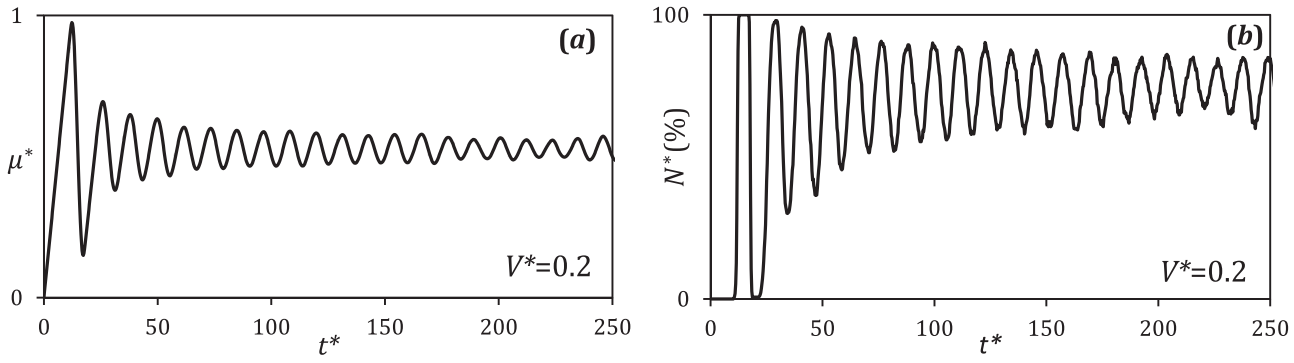

Fig. 7. : Transition from static to kinetic phase with respect to dimensionless time, t^*, for a high value of dimensionless velocity, V^*= 0.2, N= 625, R^*= 0.5, Ω^*= 0.1, and σ_s^*=σ_k^*= 0.05. *a*) dimensionless static coefficient, *b*) percentage of sliding blocks.

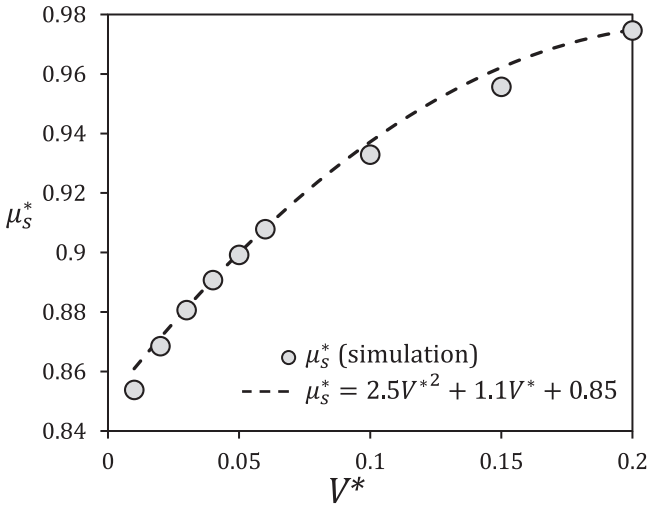

Fig. 8. : The effect of dimensionless velocity, V^*, on the dimensionless static friction coefficient, μ_s^* (N=625, R^*=0.5, Ω^*=0.1, and σ_s^*=σ_k^*=0.05). Note: □τ_c^*= 0, ■ τ_c^*= 1.

minimums and the latter specifies the value of these local minimums relative to the mean value, $\overline{\mu}_s$. In order to make a better insight, variation of dimensionless static friction, μ_s^*, versus dimensionless static standard deviation, σ_s^*, for different values of V^* is plotted in Fig. 12. Every simulation is done for five different random distributions of local friction coefficients and the mean value is presented and it is noted that the maximum of deviation observed in the obtained values of μ_s^* is less than 0.015. Nevertheless, increasing σ_s^* shows a remarkable reduction in μ_s^*, regardless of the value of V^*. The reason is that reduction in the value of

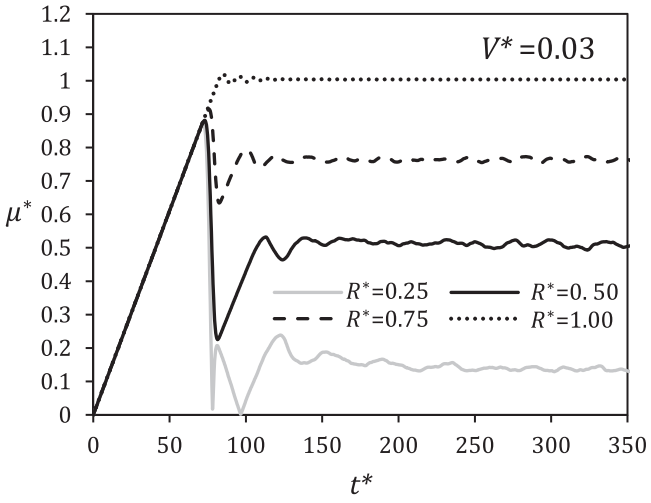

Fig. 10. : Effect of dimensionless kinetic to static friction coefficient ratio, R^*, on the transition from static to kinetic phase with respect to dimensionless time, t^*, for V^*= 0.03, N= 625, Ω^*= 0.1, and σ_s^*=σ_k^*= 0.05.

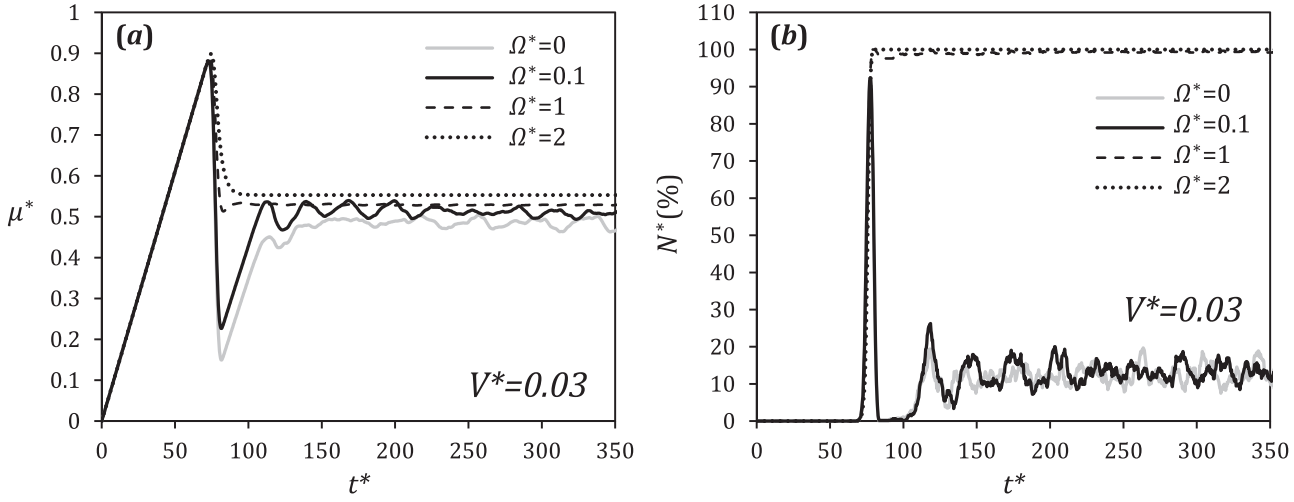

Fig. 9. : Effect of damping parameter on the transition from static to kinetic phase with respect to dimensionless time, t^* for V^*= 0.03, N= 625, R^*= 0.5, and σ_s^*=σ_k^*= 0.05. *a*) dimensionless static coefficient, *b*) percentage of sliding blocks.

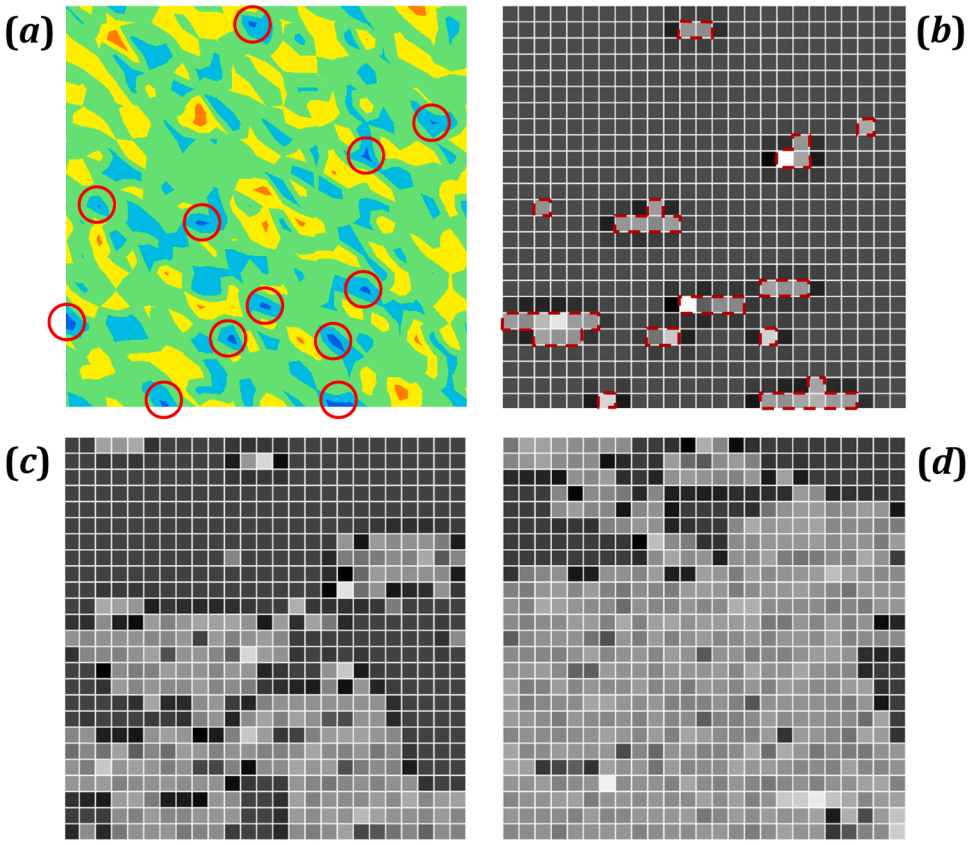

Fig. 11. : Propagation of micro-slip fronts on the contacting surface. *a*) distribution of local static friction coefficient, μ_{si}, the blue zones (in colored version) marked by circles are the local minimums of μ_{si}, *b*) the starting zones of micro-sliding, *c*) and *d*) propagation of micro-sliding. Note: □τ_c^*= 0, ■ τ_c^*= 1.

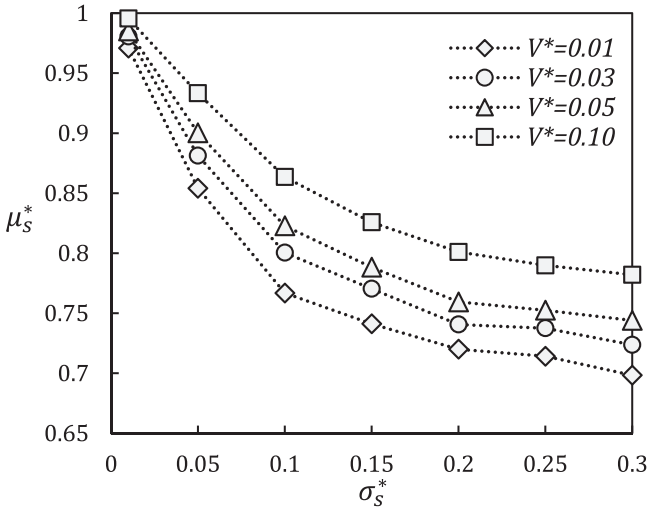

Fig. 12. : Variation of dimensionless static friction coefficient, μ_s^*, versus dimensionless static standard deviation, σ_s^*, for different values of V^* (N=625, Ω^*=0.1, and R^*=0.5).

local minumums μ_{si} facilates the start of micro-slidings. It is also notable that for low values of σ_s^*, ($\mu_{si}\rightarrow\overline{\mu}_s$), the μ_s^* approaches one, which means the global static coefficient of slider tends to mean value of local static friction coefficient, ($\mu_s^*\rightarrow\overline{\mu}_s$). For the lowest limit of $\sigma_s^*\rightarrow$0, all the blocks slide simultaneously and the concept of micro-sliding fronts does not apply. The standard deviation of local kinetic friction coefficient, σ_k^*, is not responsible for the static and transition phases and only affects the random fluctuations around μ_k^* in the kinetic phase due to stick-slip phenomenon. Finally, it is worth nothing that the standard deviations σ_s^* and σ_k^* are the main parameters that reflect the micro-roughness of the surface and can be implemented advisedly to calibrate simulations to experiments. Here, the values of σ_s^*=σ_k^*= 0.05 are adopted for all the presented results, unless otherwise stated.

3.2. Micro-textured contact surface

In the following, we put forth the effect of micro-texturing on the transition from static to kinetic friction. The micro-texturing is implemented to the model by setting to zero the local static and kinetic friction coefficients for the blocks located in the textured zone (μ_{si}=μ_{ki}=0). To gain a desirable resolution for modeling complex texturing geometries, a network of 50 × 50 blocks, resulting in a sliding area of 2500 square microns, is selected. The percentage of micro-texturing, A^*, the main characteristic parameter of micro-texturing, is defined as the ratio of micro-textured area, A_{tex}, to the total sliding area, A_{tot}:

$$A^*(\%) = 100(A_{tex}/A_{tot}) \tag{15}$$

The percent of reduction in μ_s^* is calculated as follows:

$$\text{Reduction } in\ \mu_s^* \quad (\%) = 100\frac{(\mu_s^*)_{nontex} - (\mu_s^*)_{tex}}{(\mu_s^*)_{nontex}} \tag{16}$$

Here, the boundary of a micro-textured single cavity, Γ, is defined as:

$$x_\Gamma = x_O + \lambda(\cos\varphi + w\cos(s\varphi)) \tag{17a}$$

$$y_\Gamma = y_O + \lambda(\sin\varphi - w\sin(s\varphi)) \tag{17b}$$

where (x_O, y_O) is the location of the orgin of single cavity, and λ controls its size. One can apply a surface texturing with a dimensionless texturing

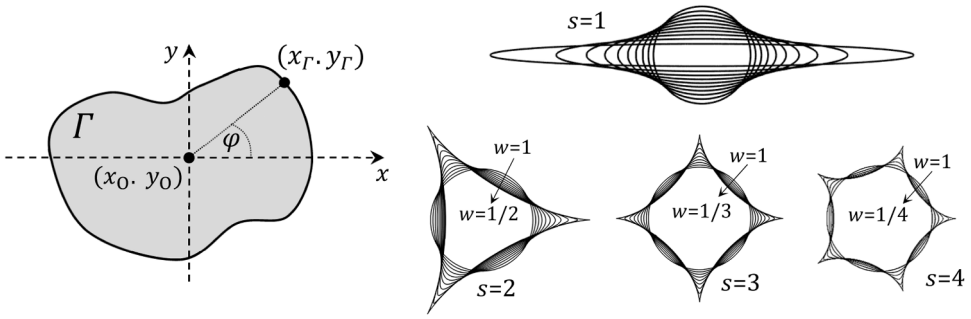

Fig. 13. : The geometrical parameters for definition of complex-micro-textured cavities.

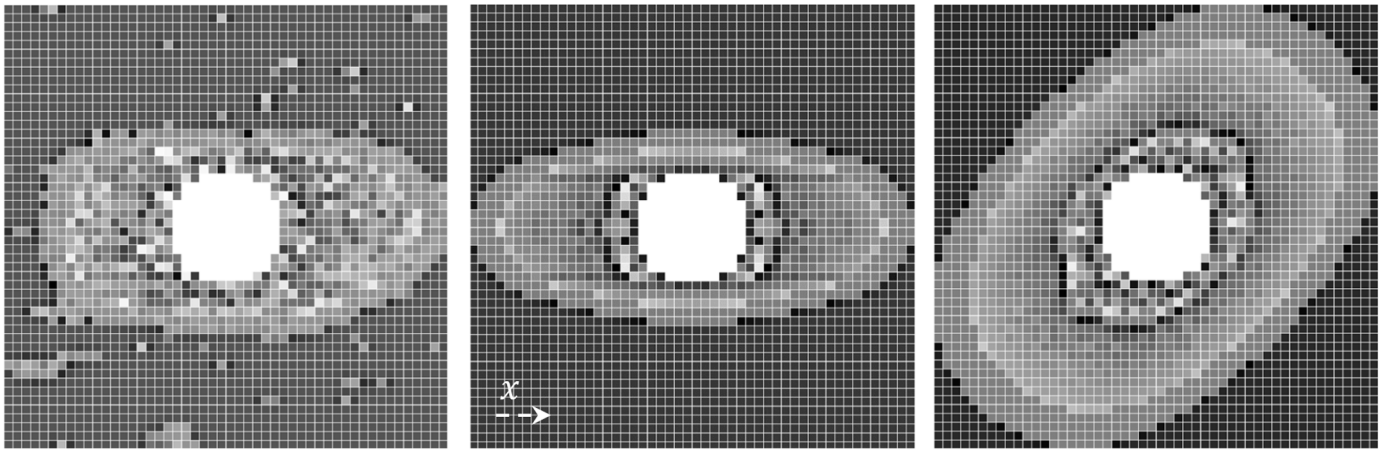

Fig. 14. : Representation of micro-sliding fronts propagation of a slider with a single circular cavity for $V^*= 0.03$, $A^*= 5\%$, $N= 2500$, $\Omega^*= 0.1$, and $R^*= 0.5$, *a*) $\sigma_s^*= 0.05$, and $V_y= 0$, *b*) $\sigma_s^*= 0$, and $V_y= 0$, *c*) $\sigma_s^*= 0$, and $V_x=V_y$. Note: □$\tau_c^*= 0$, ■ $\tau_c^*= 1$.

percentage, A^*, on a contact surface which is discritized by N blocks of length l, by setting the controlling papameter, λ, to a corresponding values, λ^*, given by:

$$\lambda^* = \sqrt{\frac{Nl^2A^*}{100\pi(1-sw^2)}} \tag{18}$$

For $s= 1$, the micro-textured cavity has an elliptical shape. When $w= 0$ it is a circle and increasing w elongates it parallel to x axis. By swaping definition of x_Γ and y_Γ, the elongation is along y axis. For $s > 1$, Eq. (17) represents a regular semi-polygons with $s+1$ curved edges. The curvature of edges is controlled by w and have the capability to alter the sharpness of $s+1$ vertexes. When $w= 0$ the sharpness is the minimum resulting in a circle cavity while for $w = 1/s$ the vortexes have the maximum of sharpness (see Fig. 13).

First, a single circular cavity with $s= 1$ and $w= 0$ located at the center of sliding area covering five percent of area, $A^* = 5\%$, is considered to find a general idea how micro-texturing may tune the transition from static to dynamic friction. Fig. (14*a*) represents the propagation of micro-sliding fronts on a sliding surface with a single circular cavity and $\sigma_s^*= 0.05$. Although the sliding fronts are influenced by local minimums of μ_{si}, however, the micro-texturing plays a significant role. For more distinction, in Fig. (14*b*) the standard deviation of local static friction coefficent is set to zero, $\sigma_s^*= 0$, to neglect the effect of the local minimums and to focus on the micro-texturing. Keeping in mind that in Fig. (14*b*) the velocity is applied along x axis, it is seen that the micro-sliding front begins from the edge of micro-texturing and propagates symetrically having a tendency to the direction of sliding velocity. It is why the fronts form an elliptical propagating path. A similar bahavior is observed in Fig. (14*c*) where the sliding velocity is applied along the orientation of 45° with respect to x axis.

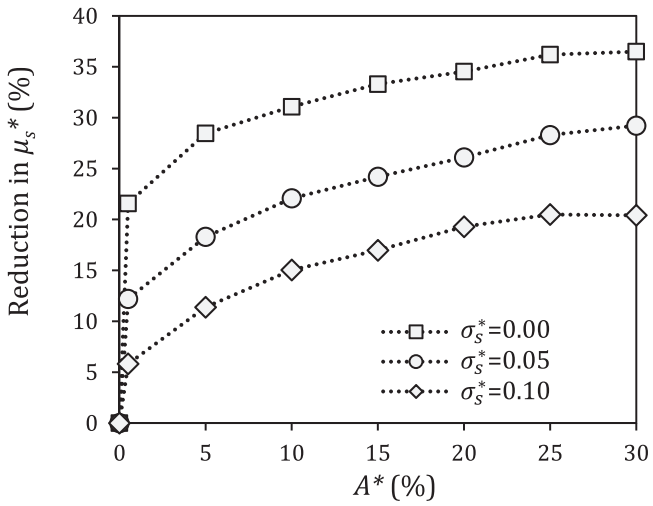

Fig. 15. : Effect of percentage of micro-texturing, A^*, of a single circular cavity on the reduction of dimensionless static friction coefficient, μ_s^*, for different values of σ_s^* (V^*=0.03, N=2500, Ω^*=0.1, R^*=0.5, and σ_s^*=0).

In Fig. 15, the percentage of reduction in μ_s^* with respect to percentage of texturing, A^*, for single circular cavity micro-texturing with different values of σ_s^* is presented. It is seen that implementation of micro-texturing decreases remarkably the static friction coefficient even for the small amount of $A^*= 1\%$. Although increasing A^* magnifies this reducing effect, however, the rate of this effect degrades. In the other word, increasing the micro-textured area, does not offer a linear reducing effect on the static friction coefficient and it gets slight

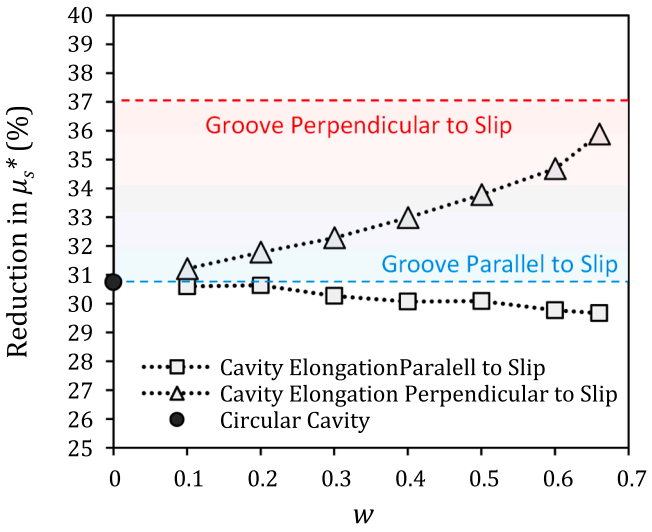

Fig. 16. : Effect of elongation of single cavity on the reduction of dimensionless static friction coefficient, μ_s^*, (V^*=0.03, A^*=10%, N=2500, Ω^*=0.1, R^*=0.5, and σ_s^*=0).

especially after A^*= 10%. Furthermore, it is seen that increasing σ_s^* attenuates the reducing effect of micro-texturing on the static friction coefficient. It results in another significant conclusion: the micro-texturing is less effective when the base non-textured surface has a topology with high standard deviation of micro-roughness. In fact, the micro-textured area behaves like a local minimum of static friction μ_{si}. It not only has a relatively large area but also includes many adjacent frictionless blocks with μ_{si}= 0. For the surfaces with small standard deviations in σ_s^*, micro-texturing leads the propagation of micro-sliding fronts and presents a remarkable reduction in μ_s^* even more than 35%. However, when σ_s^* get larger, the surface has originally a lot of starting points for micro-sliding and consequently there is low aptitude for extra reduction in μ_s^*. It means that the micro-texturing technique is more efficient for tuning frictional behavior of surfaces with more uniform micro/topology.

Fig. 16 probes the effect of elongation of micro-textured cavity with respect to the direction of sliding on dimensionless static friction coefficient, μ_s^* for a constant value of dimensionless texturing percentage, A^*= 10%. To put under focus the influence of micro-texturing, the standard deviation is set to zero, σ_s^*= 0. For a circular cavity, the reduction in μ_s^* is around 31% and it is observed that elongation of cavity perpendicular to the sliding direction can improve slightly this reducing effect to reach 37% for a groove perpendicular to the sliding direction. Nevertheless, elongation parallel to the sliding direction shows an inappreciable opposite effect. It is noted that a groove parallel to sliding direction behaves similar to a circular cavity of the same A^*. Fig. 17

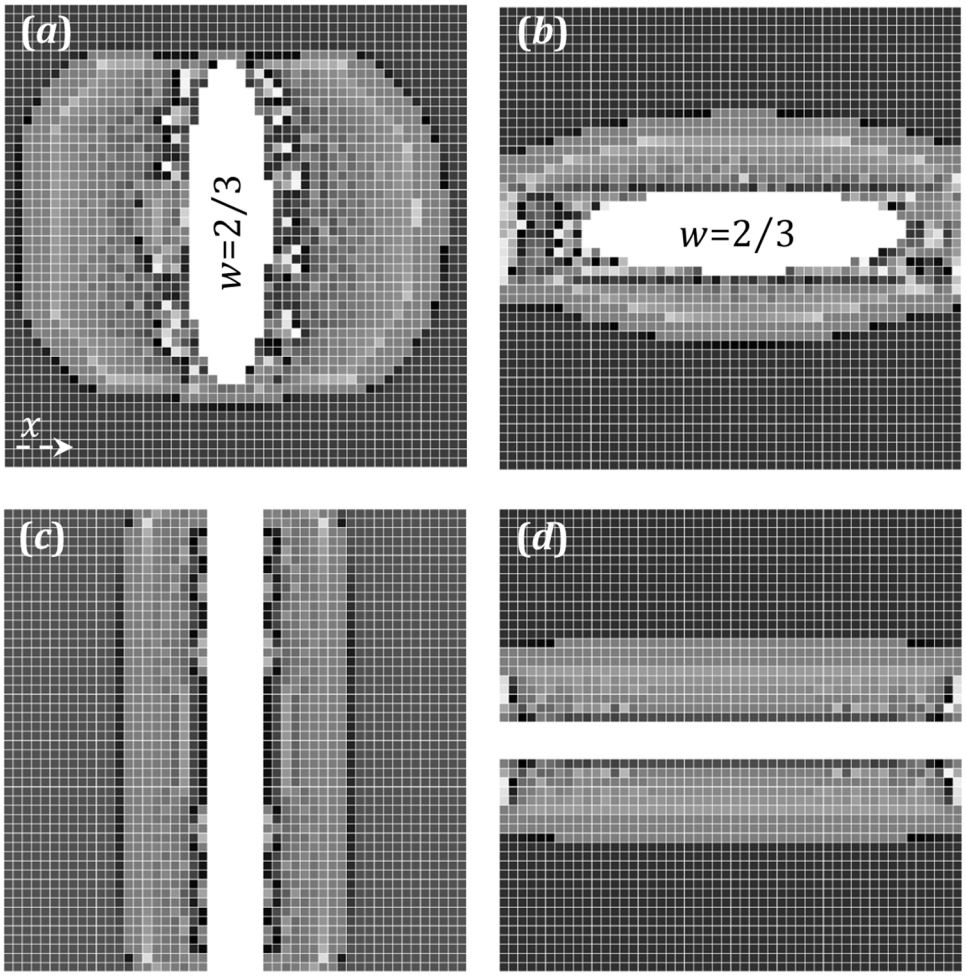

Fig. 17. : Distribution of dimensionless contact stress, τ_c^*, of a micro-textured sliding surface for V^*= 0.03, A^*= 10%, N= 2500, Ω^*= 0.1, R^*= 0.5 and σ_s^*= 0. *a*) cavity elongated perpendicular to the sliding direction, *b*) cavity elongated parallel to the sliding direction, *c*) groove elongated perpendicular to the sliding direction, *d*) groove elongated parallel to the sliding direction. Note: □τ_c^*= 0, ■ τ_c^*= 1.

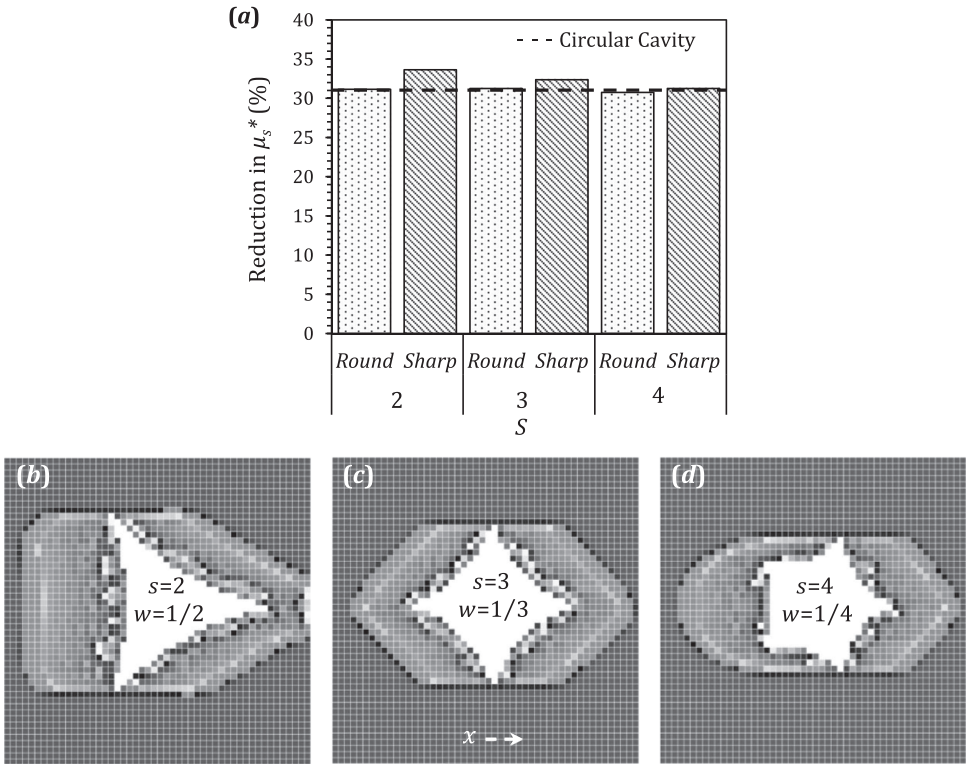

Fig. 18. : Effect of the shape of micro-textured single cavity for $V^*=0.03$, $A^*=10\%$, $N=2500$, $\Omega^*=0.1$, $R^*=0.5$, and $\sigma_s^*=0$, *a*) percentage of reduction in dimensionless static friction coefficient, μ_s^*, *b-e*) Distribution of dimensionless contact stress, τ_c^*. Note: □$\tau_c^*=0$, ■ $\tau_c^*=1$.

represents the distribution of dimensionless contact stresses corresponding to Fig. 16.

Fig. 18 draws attention to the shape of micro-textured cavities. Six different shapes are modeled to see the effect of number and sharpness of the vertexes: semi-triangle (s=2), semi-square (s=3), and semi-pentagon (s=4), each has two different sharpness' named: *Sharp* ($w=1/s$), and *Round* ($w=1/(5s)$). From Fig. (18*b*) one can conclude that neither number nor sharpness of the vertexes does present a notable effect on μ_s^*. In the other word, unlike the propagation of cracks through an elastic media, propagation of micro-sliding fronts on the contacting surface is much less sensitive to the singularity in geometry. Note that engraving complex patterns increases the micro-texturing cost, in comparison to a simple circular cavity.

4. Conclusion

Present work investigates the capability of micro-texturing for tuning the transition from static to kinetic friction via a two-dimensional lattice spring-block model [21] based on local classical Amontons–Coulomb friction force assumptions. The conclusions are listed as follows:

- Micro-texturing significantly decreases the static friction coefficient even for a small amount of covering percentage like 1%. However, for covering percentage larger than 10% the rate of this effect reduces.
- It is found that micro-texturing process is more efficient for tuning frictional behavior of surfaces with lower standard deviation in local static friction coefficients. In other words, surfaces presenting more uniformity in micro topologies are better candidates for micro-texturing.
- Selecting micro-texturing patterns which are more elongated perpendicular to the sliding direction can improve slightly its reducing effect on static friction coefficient. The effect of shape of micro-sized semi-polygonal cavities in terms of number of edges and sharpness of vertexes are studied and simulations reveal that the effect of shape slightly affect the frictional response.

Declaration of Competing Interest

No competing interest.

Data availability

No data was used for the research described in the article.

Acknowledgments

This work was supported by The LIFE programme, Project Title: High performance devulcanized masterbatches for End-of-Life Tire reuse in high-volume technical compounding applications (LIFE GREEN VULCAN, LIFE19 ENV/IT/000213). https://www.lifegreenvulcan.eu/.

References

[1] Persson BNJ. Sliding Friction: Physical Principles and Applications. 2nd ed..,. Berlin, Heidelberg: Springer Berlin Heidelberg,; 2000.
[2] Gillmor CS. Coulomb and the Evolution of Physics and Engineering in Eighteenth-Century France. Princeton: Princeton University Press,; 1971.
[3] Coulomb CA. Theorie des machines simple (Theory of simple machines). Paris: Bachelier,; 1821.
[4] Dieterich JH. Modeling of rock friction: 1. experimental results and constitutive equations. J Geophys Res 1979;84(B5):2161. https://doi.org/10.1029/JB084iB05p02161.
[5] Ruina A. Slip instability and state variable friction laws. J Geophys Res Solid Earth 1983;88(B12):10,359–10,370. https://doi.org/10.1029/JB088iB12p10359.
[6] Bhushan B. Nanotribology and nanomechanics of MEMS/NEMS and BioMEMS/BioNEMS materials and devices. Micro Eng 2007;84:387–412.
[7] Filippov A, Popov VL, Gorb SN. Shear induced adhesion: contact mechanics of biological spatula-like attachment devices. J Theor Biol 2011;276:126–31.
[8] Labonte D, Williams JA, Federle W. Surface contact and design of fibrillar 'friction pads' in stick insects (Carausius morosus): mechanisms for large friction coefficients and negligible adhesion. J R Soc Interface 2014;11:20140034.

[9] Prevost A, Scheibert J, Debregeas G. Effect of fingerprints orientation on skin vibrations during tactile exploration of textured surfaces. Commun Integr Biol 2009;2:422–4.
[10] Scheibert J, Leurent S, Prevost A, Debregeas G. The role of fingerprints in the coding of tactile information probed with a biomimetic sensor. Science 2009;323:1503–6.
[11] Murarash B, Itovich Y, Varenberg M. Tuning elastomer friction by hexagonal surface patterning. Soft Matter 2011;7:5553–7.
[12] Borghi A, Gualtieri E, Marchetto D, Moretti L, Valeri S. Tribological effects of surface texturing on nitriding steel for high-performance engine applications. Wear 2008;265:1046–51.
[13] Jabbarzadeh A, Atkinson JD, Tanner RI. Effect of the wall roughness on slip and rheological properties of hexadecane in molecular dynamics simulation of Couette shear flow between two sinusoidal walls. Phys Rev E 2000;61:690–9.
[14] Xiaozhu Zh, Boey F, Huo F, Huang L, Zhang H. Chemically functionalized surface patterning. Small 2011;7(16):2273–89. https://doi.org/10.1002/smll.201002381.
[15] Mao B, Siddaiah A, Liao Y, Menezes PL. Laser surface texturing and related techniques for enhancing tribological performance of engineering materials: a review. J Manuf Process 2018;53:153–73.
[16] Bandyopadhyay A, Heer B. Additive manufacturing of multi-material structures. Mater Sci Eng R Rep 2018;129:1–16.
[17] Sheng X, et al. Multi-material 3D printing of caterpillar-inspired soft crawling robots with the pneumatically bellow-type body and anisotropic friction feet. Sens Actuators A Phys 2020;316:112398.
[18] Capozza R, Urbakh M. Static friction and the dynamics of interfacial rupture. Phys Rev B 2012;86:085430.
[19] Amundsen DS, et al. 1D model of precursors to frictional stick-slip motion allowing for robust comparison with experiments. Tribol Lett 2012;45(2):357–69.
[20] Trømborg J, et al. Speed of fast and slow rupture fronts along frictional interfaces. Phys Rev E 2015;92:012408.
[21] Costagliola G, Bosia F, Pugno N. A 2-D model for friction of complex anisotropic surfaces. J Mech Phys Solids 2018;112:50–65.
[22] Costagliola G, Bosia F, Pugno N. Correlation between slip precursors and topological length scales at the onset of frictional sliding. Int J Solids Struct 2022;243:111525.
[23] Berardo A, et al. An experimental-numerical study of the adhesive static and dynamic friction of micro-patterned soft polymer surfaces. Mater Des 2019;181:107930.
[24] Costagliola G, Bosia F, Pugno N. Tuning friction with composite hierarchical surfaces. Tribol Int 2017;115:261–7.
[25] Guarino R, et al. Evidence of friction reduction in laterally graded materials. Belisten J Nanotechnol 2018;9:2443–56.
[26] Capozza R, Pugno N. Effect of surface grooves on the static friction of an elastic slider. Tribol Lett 2015;58:35.
[27] Costagliola G, Bosia F, Pugno N. Static and dynamic friction of hierarchical surfaces. Phys Rev E 2016;94:063003.
[28] Costagliola G, Bosia F, Pugno N. Tuning of frictional properties in torsional contact by means of disk grading. Friction 2022;10(5):787–802.
[29] Ostoja-Starzewski M. Lattice models in micromechanics. Appl Mech Rev 2002;55(1):1.
[30] Rubinstein SM, Cohen G, Fineberg J. Detachment fronts and the onset of dynamic friction. Nature 2004;430:1005–9.
[31] Jacobs TD, Martini A. Measuring and understanding contact area at the nanoscale: a review. Appl Mech Rev 2017;69(6):060802.
[32] Ciavarella M, Papangelo A. Discussion of “measuring and understanding contact area at the nanoscale: a review”. Appl Mech Rev 2017;69(6):065502.
[33] Vakis AI, et al. Modeling and simulation in tribology across scales: an overview. Tribol Int 2018;125:169–99.
[34] Braun OM, Barel I, Urbakh M. Dynamics of transition from static to kinetic friction. Phys Rev Lett 2009;103:194301.
[35] Trømborg J, et al. Transition from static to kinetic friction: insights from a 2D model. Phys Rev Lett 2011;107:074301.
[36] Capozza R, et al. Stabilizing stick-slip friction. Phys Rev Lett 2011;107:024301.
[37] Absi E, Prager W. A comparison of equivalence and finite element methods. Comput Methods Appl Mech Eng 1975;6(1):59–64.
[38] Cundall PA, Strack ODL. A discrete numerical model for granular assemblies. Geotechnique 1979;29:47–65.
[39] Allen MP, Tildesley DJ. Computer Simulation of Liquids. Oxford: Oxford Science Publ,; 1989.